Mergos, P.E. & Kappos, A. J. (2013). Damage Analysis of Reinforced Concrete Structures with Substandard Detailing. In: M. Papadrakakis, M. Fragiadakis & V. Plevris (Eds.), Computational methods in earthquake engineering: Volume 2. Computational Methods in Applied Sciences, 30. (pp. 149-176). Springer. ISBN 978-94-007-6572-6

Damage Analysis of Reinforced Concrete Structures with Substandard Detailing

Panagiotis E. Mergos[1] **and Andreas J. Kappos**[2*]

[1]Research Associate, Laboratory of Concrete and Masonry Structures,

Department of Civil Engineering, Aristotle University of Thessaloniki, 54124 Greece,

Email address: panmerg@yahoo.com

[2]Professor, Laboratory of Concrete and Masonry Structures,

Department of Civil Engineering, Aristotle University of Thessaloniki, 54124 Greece,

[*]Corresponding author: ajkap@civil.auth.gr

Keywords Finite Element Model, Reinforced Concrete, Shear-Flexure Interaction, Bond-Slip, Substandard Detailing.

Abstract The goal of this study is to investigate seismic behaviour of existing R/C buildings designed and constructed in accordance with standards that do not meet current seismic code requirements. In these structures, not only flexure, but also shear and bond-slip deformation mechanisms need to be considered, both separately and in combination. To serve this goal, a finite element model is developed for inelastic seismic analysis of complete planar R/C frames. The proposed finite element is able to capture gradual spread of inelastic flexural and shear deformations as well as their interaction in the end regions of R/C members. Additionally, it is capable of predicting shear failures caused by degradation of shear strength in the plastic hinges of R/C elements, as well as pullout failures caused by inadequate anchorage of the reinforcement in the joint regions. The finite element is fully implemented in the general inelastic finite element code IDARC2D and it is verified against experimental results involving individual column and plane frame specimens with non-ductile detailing. It is shown that, in all cases, satisfactory correlation is established between the model predictions and the experimental evidence. Finally, parametric studies are conducted to illustrate the significance of each deformation mechanism on the seismic response of the specimens under investigation. It is concluded, that all deformation mechanisms, as well as their interaction, should be taken into consideration in order to predict reliably seismic damage of R/C structures with substandard detailing.

1 Introduction

In countries often struck by devastating earthquakes, a large fraction of the existing R/C building stock has not been designed to conform to modern seismic codes. These structures have not been detailed in a ductile manner and according to capacity design principles. Therefore, it is likely, that in case of a major seismic event, their structural elements will suffer from brittle types of failure, which may lead to irreparable damage or collapse of the entire structure.

The first step in performing a realistic seismic damage analysis is to develop an analytical model that is able to predict accurately inelastic response to seismic loading. The complexity of this problem increases significantly for non-ductile R/C structures, where, apart from flexure, shear and anchorage slip may significantly influence the final response. This is the reason why, especially for these structures, all three deformation mechanisms should be explicitly treated, while their interaction should also be taken into consideration [1].

Current research on seismic assessment of R/C structures is focused primarily on flexural response. Deformations caused by shear and bond-slip related mechanisms are either ignored or lumped into flexure [2]. However, the necessary assumptions inherent to both of these approaches may drive the assessment procedure to erroneous results. This is especially the case for 'old type' existing R/C structures, where shear and bond types of failure cannot be precluded, due to the absence of ductile detailing and capacity design.

Only a small number of studies [3-7] proposed numerical models for seismic assessment of non-ductile R/C structures, where all three deformation mechanisms are considered individually. Nevertheless, all these studies have demonstrated the importance and the advantages of treating separately all deformation components, when assessing seismic response of deficient R/C structures.

Following this approach, a new finite element model [8-11] is developed herein for examining inelastic response of R/C frames with substandard detailing. The novel feature of the proposed finite element is the fact that it is capable of modelling gradual spread of inelastic flexural and shear deformations, as well as their interaction in the end regions of R/C members. Furthermore, it is able to predict shear failures caused by degradation of shear strength in the plastic hinges of R/C elements, as well as pullout failures caused by inadequate anchorage of the reinforcement in the joint regions under general loading conditions.

The chapter starts with an analytical description of the finite element model. The element formulation, components and inherent assumptions are explained. Emphasis is placed on the ability of the numerical model to predict brittle types of failure (i.e. shear and bond). In addition, the necessary alterations to the nonlinear solution algorithms are discussed in order for the proposed beam-column element to be fully implemented in a general inelastic damage analysis finite element code.

Then, with the aim to verify the capabilities of the proposed numerical model to reproduce inelastic response of R/C buildings with deficient configuration, the proposed finite element is applied to the analysis of well documented R/C column

and frame specimens subjected to cyclic or seismic loading. Analytical results are compared with experimental recordings. It is shown that the numerical model is able to capture sufficiently experimental response in terms of strength, stiffness and displacements, and to predict reliably the prevailing mode of failure for each specimen.

Finally, parametric analyses illustrate the relative importance of each deformation mechanism on the response of the examined specimens in the elastic and inelastic range. It is shown that proper modelling of all flexibility components, as well as their interaction, is a substantial prerequisite for reliable prediction of seismic response of R/C frames built with inadequate earthquake resistant provisions.

2 Finite Element Model

2.1 General formulation

The finite element model proposed herein for seismic damage analysis of existing RC structures is based on the flexibility approach (force-based element) and belongs to the class of phenomenological models. It consists of three sub-elements representing flexural, shear, and anchorage slip response (Fig. 1). The total flexibility matrix F_b is calculated as the sum of the flexibilities of its sub-elements and can be inverted to produce the element stiffness matrix K_b. Hence:

$$F_b = F^{fl} + F^{sh} + F^{sl} \tag{1}$$

Where, F_b, F^{fl}, F^{sh}, F^{sl} are the basic total, flexural, shear and anchorage slip, respectively, tangent flexibility matrices. K_b is the basic tangent stiffness matrix of the element, relating incremental moments ΔM_A, ΔM_B and rotations $\Delta\theta_A$, $\Delta\theta_B$ at the element flexible ends A and B respectively.

The local stiffness matrix K_e, relating displacements and forces at the element joints, is easily determined following standard structural analysis procedures. The components of the examined finite element, as well as their interaction, are described analytically in the following sections.

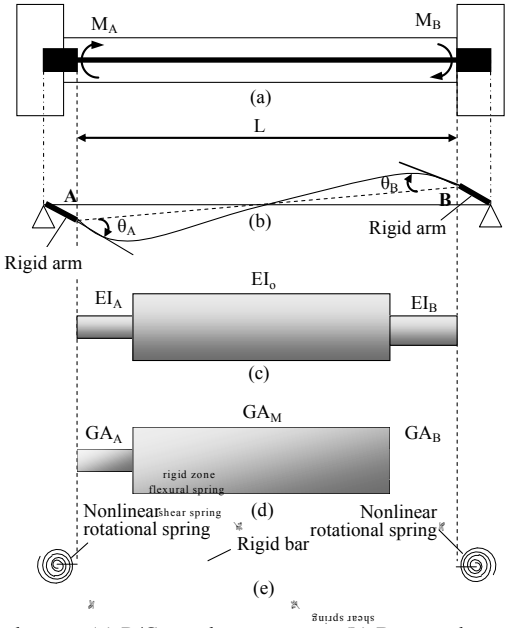

Fig. 1 Proposed finite element. **(a)** R/C member geometry. **(b)** Beam-column finite element with rigid arms. **(c)** Flexural sub-element. **(d)** Shear sub-element. **(e)** Anchorage slip sub-element

2.2 Flexural sub-element

This sub-element (Fig. 1c) is used for modelling flexural behaviour of an R/C member before and after yielding of the longitudinal reinforcement. It consists of a set of rules governing the hysteretic moment-curvature (M-φ) response of the member end sections and a spread inelasticity model describing flexural stiffness distribution along the entire member.

M-φ hysteretic model (Fig. 2a) is composed by the skeleton curve and a set of rules determining response during loading, unloading and reloading. M-φ envelope curve is derived by section analysis and appropriate bilinearization. Loading response is assumed to follow the bilinear envelope curve. Unloading is based on the respective Sivaselvan & Reinhorn [12] hysteretic rule adjusted for mild stiffness degradation. Reloading aims at the point with previous maximum excursion in the opposite direction.

To capture distribution of section flexural stiffness along the concrete member, a gradual spread inelasticity model is assigned [13]. Following this model, the element is divided into two inelastic end regions and one elastic intermediate zone. Stiffness along the intermediate zone is assumed to be uniform and equal to the elastic stiffness EI_o of the M-φ envelope curve.

Stiffness distribution inside the inelastic zones depends on the loading state of the end section hysteretic response. In particular, Fig. 2b illustrates hysteretic response of four discrete sections located inside one plastic hinge region. It can be

seen that when all sections remain in the strain hardening branch (loading state), flexural stiffness remains constant in the inelastic zone. However, when they are in the unloading and reloading state, stiffness varies from a minimum value $r \cdot EI_o$ ($0 \le r \le 1$), corresponding to the end section, to a maximum value, which is equal to EI_o. Hence, under the general assumption that the loading state of all sections of the yielded region remains the same, it may be considered that when M-φ end section hysteretic response is on the strain hardening branch, stiffness distribution remains uniform in the inelastic zone. In the case where end-section M-φ behaviour is in the unloading or reloading state, it is assumed that the stiffness varies linearly from end section flexural stiffness $r_1 \cdot EI_o$ or $r_2 \cdot EI_o$ to EI_o.

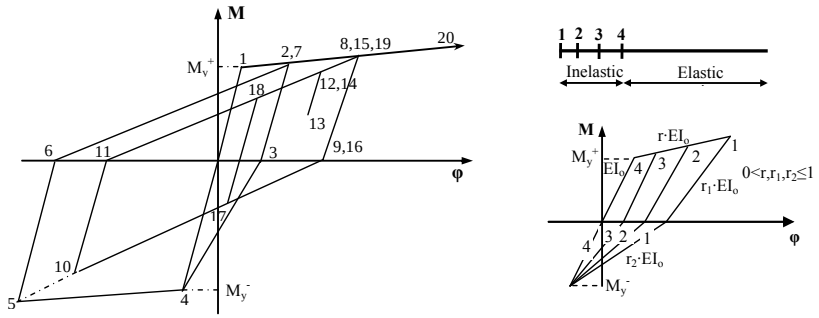

Fig. 2 (a) M-φ hysteretic model. **(b)** M-φ hysteretic response of four individual sections inside plastic hinges

In accordance with the previous observations, stiffness distribution along the member may be assumed to have one of the shapes shown in Fig. 3, where L is the length of the member; EI_o is the stiffness at the intermediate part of the element and EI_A and EI_B are the current flexural rigidities of the sections at the ends A and B respectively. The flexural rigidities EI_A and EI_B are determined from the M-φ hysteretic relationship of the corresponding end sections.

In the same figure, α_A and α_B are the yield penetration coefficients. The yield penetration coefficients specify the proportion of the element where the acting moment exceeds the end-section yield moment. These coefficients are first calculated for the current moment distribution from Eq. 2, where M_{yA} and M_{yB} are the respective flexural yielding moments of end sections A and B. Then, they are compared with the previous maximum penetration lengths; the yield penetration lengths cannot be smaller than their previous maximum values.

$$\alpha_A = \frac{M_A - M_{yA}}{M_A - M_B} \le 1 \; ; \; \alpha_B = \frac{M_B - M_{yB}}{M_B - M_A} \le 1 \qquad (2)$$

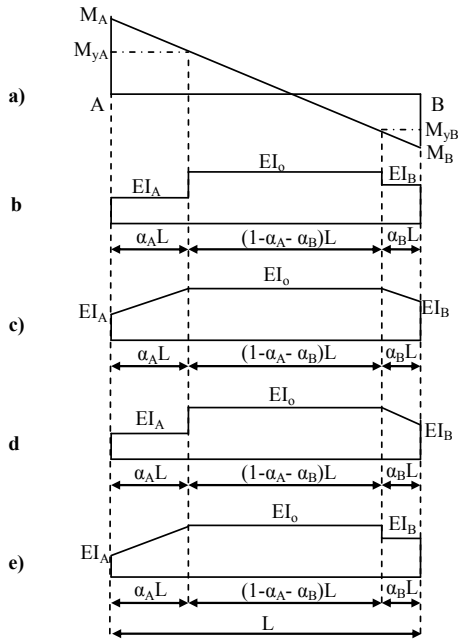

Fig. 3 Element. **(a)** Bending moment diagram. **(b)** Stiffness distribution when ends A and B are in the loading state. **(c)** Stiffness distribution when ends A and B are in the unloading or reloading state. **(d)** Stiffness distribution when end A is in the loading and end B is in the unloading or reloading state. **(e)** Stiffness distribution when end A is in the unloading or reloading state and end B is in the loading state

Table 1 Determination of flexural flexibility matrix coefficients.

Flexibility coefficient	Stiffness distribution	c_o	c_A	c_B
f_{11}	Fig. 3b	4	$12\alpha_A -12\alpha_A^2+4\alpha_A^3$	$4\alpha_B^3$
f_{22}	Fig. 3b	4	$4\alpha_A^3$	$12\alpha_B -12\alpha_B^2+4\alpha_B^3$
f_{12}	Fig. 3b	-2	$4\alpha_A^3-6\alpha_A^2$	$4\alpha_B^3-6\alpha_B^2$
f_{11}	Fig. 3c	4	$6\alpha_A -4\alpha_A^2+\alpha_A^3$	α_B^3
f_{22}	Fig. 3c	4	α_A^3	$6\alpha_B -4\alpha_B^2+\alpha_B^3$
f_{12}	Fig. 3c	-2	$\alpha_A^3-2\alpha_A^2$	$\alpha_B^3-2\alpha_B^2$
f_{11}	Fig. 3d	4	$12\alpha_A -12\alpha_A^2+4\alpha_A^3$	α_B^3
f_{22}	Fig. 3d	4	$4\alpha_A^3$	$6\alpha_B -4\alpha_B^2+\alpha_B^3$
f_{12}	Fig. 3d	-2	$4\alpha_A^3-6\alpha_A^2$	$\alpha_B^3-2\alpha_B^2$
f_{11}	Fig. 3e	4	$6\alpha_A -4\alpha_A^2+\alpha_A^3$	$4\alpha_B^3$
f_{22}	Fig. 3e	4	α_A^3	$12\alpha_B -12\alpha_B^2+4\alpha_B^3$
f_{12}	Fig. 3e	-2	$\alpha_A^3-2\alpha_A^2$	$4\alpha_B^3-6\alpha_B^2$

Having established the stiffness distribution along the R/C member at each step of the analysis, the coefficients of the flexibility matrix of the flexural sub-element can be derived from the general Eq. 3 and Table 1, determined by applying the principle of virtual work.

$$f_{ij}^{fl} = \frac{L}{12EI_o}\left(c_o + c_A \cdot \gamma_A + c_B \cdot \gamma_B\right);\ \gamma_A = \frac{EI_o}{EI_A} - 1;\ \gamma_B = \frac{EI_o}{EI_B} - 1 \qquad (3)$$

2.3 Shear sub-element

The shear sub-element (Fig. 1d) represents the hysteretic shear behaviour of the R/C member prior and subsequent to shear cracking, flexural yielding, and yielding of the shear reinforcement. Herein, this sub-element has been designed in a similar way to the flexural element described above. It consists of a set of rules determining V-γ (shear force vs. shear strain) hysteretic behaviour of the member intermediate and end regions, and a shear spread inelasticity model determining distribution of shear stiffness along the R/C member.

Shear hysteresis is determined by the V-γ skeleton curve and a set of rules describing response during unloading and reloading. The primary curve is first derived without considering shear-flexure interaction effect. This initial envelope curve (Fig. 4) is valid for modelling shear behaviour outside plastic hinge regions of the R/C members.

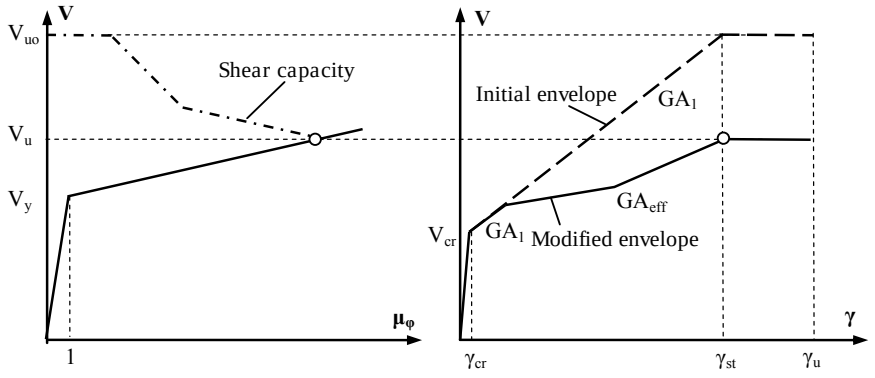

Fig. 4 (a) Flexural primary curve in terms of member shear force and curvature ductility demand of the critical cross section. **(b)** Shear (V – γ) primary curve before and after modelling shear-flexure interaction

The V-γ initial primary curve consists of four branches (Fig. 4), but only three different slopes, as explained later on. The first branch connects the origin and the shear cracking point, which is defined as the point where the nominal principal tensile stress exceeds the mean tensile strength of concrete [14]. The second and third branches of the initial primary curve have the same slope and connect the shear cracking point to the point corresponding to the onset of yielding of trans-

verse reinforcement, or else the point of attainment of maximum shear strength (γ_{st}, V_{uo}). The second and third branches are separated at the point corresponding to flexural yielding (γ_y,V_y). This approach is adopted in order to distinguish hysteretic shear behaviour before and after flexural yielding [8].

Initial shear strength V_{uo} is calculated by the Priestley et al. [15] approach for curvature ductility demand $\mu_\varphi \leq 3$ (i.e. no strength degradation). Shear strain at stirrup yielding γ_{st} is evaluated by the truss analogy approach and two modification factors for the member aspect ratio and normalized axial load, as proposed by the writers of this study [11] on the basis of calibration studies with the experimental evidence.

The fourth branch is almost horizontal and describes shear response after yielding of transverse reinforcement and until onset of shear failure, corresponding to shear distortion γ_u. The latter distortion is established on the basis of an empirical formula proposed by the writers of this study [11] derived by experimental results coming from 25 R/C specimens failing in shear mode. The proposed formula connects γ_u with the level of the applied axial load, the amount of transverse reinforcement and the member shear-span.

Several studies [14-16] have demonstrated that shear strength degrades due to disintegration of the plastic hinge zones caused by inelastic flexural deformations. Furthermore, it has been shown experimentally [17,18] that shear distortions in the plastic hinge regions may increase rapidly ("shear-flexural yielding") subsequent to flexural yielding, despite the fact that shear force demand remains almost constant, as it is controlled by flexural yielding. The combination of these phenomena is defined herein as shear-flexure interaction effect.

In this study, a new analytical methodology is proposed for the calculation of the modified V-γ envelope curve, which accounts properly for shear-flexure interaction effect (Fig. 4). The modified envelope is employed by the proposed finite element model for the determination of shear hysteretic response inside the locations of the plastic hinges.

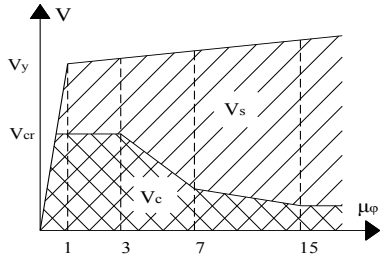

Fig. 5 Variation of shear resisting mechanisms with μ_φ in plastic hinges

In accordance with truss analogy approach [19], after shear cracking, shear strain increment $\Delta\gamma_s$ is related to the additional shear force resisted by the truss mechanism ΔV_s by Eq. 4, where GA_1 is the cracked stiffness of the initial shear primary curve shown in Fig. 4.

$$\Delta\gamma_s = \frac{\Delta V_s}{GA_1} \tag{4}$$

Figure 5 illustrates variation of capacity of shear resisting mechanisms (concrete V_c and truss V_s) in the plastic hinge region of a single R/C member following the Priestley et al. [15] shear strength approach (for clarity, contribution of axial load is lumped into V_c). It can be seen that after μ_φ>3, V_s increases to accommodate both additional shear demand ΔV and additional deterioration of the concrete resisting mechanism $\Delta degV_c$. Hence, ΔV_s can be considered as the sum of ΔV and $\Delta degV_c$.

$$\Delta V_s = \Delta V + \Delta\, deg\, V_c \tag{5}$$

If GA_{eff} is the tangent stiffness of the modified shear primary curve including shear-flexure interaction effect, by definition, it yields the same increment of shear distortions $\Delta\gamma_s$ only for the applied shear force increment ΔV (without $\Delta degV_c$), as illustrated in Fig. 6. Consequently

$$\Delta\gamma_s = \frac{\Delta V}{GA_{eff}} \tag{6}$$

Combining Eqs. 4-6, Eq. 7 is derived for determining stiffness of the shear envelope curve after yielding in flexure. This formula shows that GA_{eff} can only be either equal or smaller than GA_1. Equality holds only when the degradation of the concrete shear resisting mechanisms is negligible.

$$GA_{eff} = \frac{\Delta V}{\Delta V + \Delta\, deg\, V_c} \cdot GA_1 \tag{7}$$

It is important to note that, following the afore-described analytical procedure, degraded shear strength V_u [15] is always attained at shear distortion γ_{st} corresponding to stirrup yielding (Fig. 4). This observation is in accordance with truss analogy approach [19].

After determination of the V-γ envelope curves, shear hysteretic response has to be established. This behaviour is generally characterized by significant stiffness degradation and pinching. In this study, the empirical model by Ozcebe and Saatcioglu [18] (Fig. 7a) is adopted for this response, properly modified by the writers [8] in order to be incorporated in the general structural analysis framework.

After determining shear hysteretic responses, shear stiffness distribution along the R/C member has to be defined. In reality, due to shear-flexure interaction and following flexural deformations, inelastic shear strains tend to spread gradually from the member ends to the mid-span as the length of inelastic zones increases.

To capture this phenomenon, a shear gradual spread inelasticity model has been first proposed by the writers of this study in [9,11]. The model aims at monitoring variation of shear stiffness along the concrete member throughout the response.

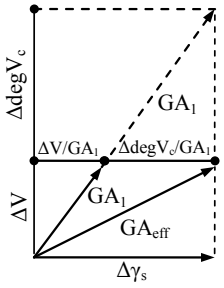

Fig. 6 Determination of effective shear stiffness GA_{eff}

To serve this goal, the shear sub-element is divided in two variable length end-zones, where shear-flexure interaction takes place, and an intermediate region where interaction with flexure may be disregarded. The lengths of the inelastic zones α_{As} and α_{Bs} of the shear sub-element are determined by the respective ones of the flexural sub-element (Fig. 7b). Hence, they are also constantly updated to capture gradual growth of the plastic hinge regions. Furthermore, the stiffness of these end-zones GA_A and GA_B are defined by the modified V-γ envelope curves (Fig. 4) calculated for the current μ_φ demands of the respective ends of the flexural sub-element in accordance with the analytical procedure described in the previous. Shear stiffness distribution is assumed uniform inside the inelastic zones since acting shear is uniform and all sections remain in the same V-γ loading state.

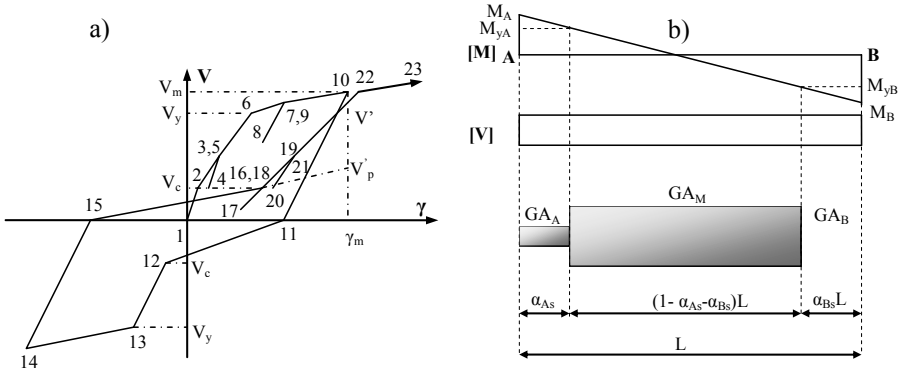

Fig. 7 (a) Shear hysteretic model. (b) Shear spread plasticity model

Shear stiffness GA_M of the intermediate part of the sub-element is also assumed uniform, but it is determined by the initial V-γ primary curve, without considering shear-flexure interaction effect.

After having established the distribution of GA along the R/C member at each step of the analysis, the coefficients of the flexibility matrix of the shear sub-element are given by Eq. 8, determined by the principle of virtual work.

$$f_{ij}^{sh} = \frac{a_{As}}{GA_A \cdot L} + \frac{1 - a_{As} - a_{Bs}}{GA_M \cdot L} + \frac{a_{Bs}}{GA_B \cdot L} \quad (i,j=1,2) \tag{8}$$

2.4 Bond-slip sub-element

The bond-slip sub-element accounts for the fixed-end rotations which arise at the interfaces of adjacent R/C members due to bond deterioration and the ensuing slippage of the reinforcement anchorage in the joint regions. The proposed model consists of two concentrated rotational springs located at the member-ends; the two (uncoupled) springs are connected by an infinitely rigid bar (Fig. 1e). Following this formulation, the coefficients of the bond-slip flexibility matrix F^{sl} are given by Eq. 9, where f_A^{sl} and f_B^{sl} are the current tangent flexibilities of the concentrated rotational springs at the ends A and B respectively. These flexibilities depend on the moment - fixed end rotation ($M\text{-}\theta_{slip}$) envelope curve and the model used to represent hysteretic behaviour of each rotational spring.

$$f_{11}^{sl} = f_A^{sl}\ ;\ f_{22}^{sl} = f_B^{sl}\ ;\ f_{12}^{sl} = f_{21}^{sl} = 0 \tag{9}$$

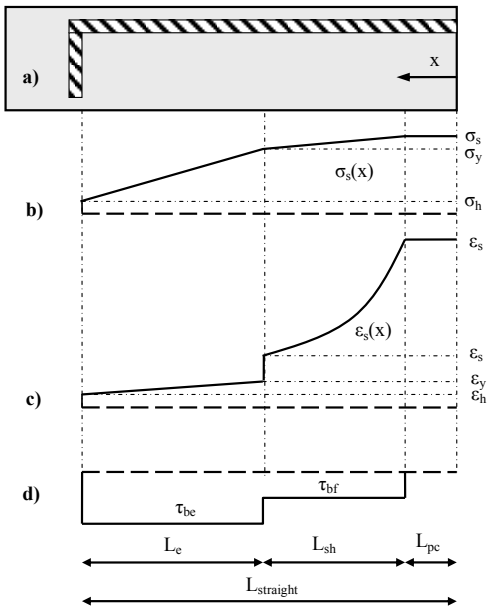

Fig. 8 (a) Reinforcing bar with 90° hook embedded in concrete. **(b)** Steel stress distribution. **(c)** Strain distribution. **(d)** Bond stress distribution

The M-θ_{slip} skeleton curve is derived on the basis of a simplified procedure [20] assuming uniform bond stress along different segments of the anchored rebar (Fig. 8). These segments are the elastic region L_e, the strain-hardening region L_{sh} and the pullout cone region L_{pc}. The average elastic bond strength τ_{be} according to ACI 408 [21] is adopted here for the elastic region, while the frictional bond τ_{bf} according to the CEB Model Code [22] is assumed to apply within the strain-hardening region. In the pullout cone region, it is assumed that the acting bond is negligible.

For various levels of the applied end moment and using the results of M-φ analysis, the stress σ_s and strain ε_s of the reinforcing bar at the loaded end are first determined. Then, from equilibrium and applying the assumed bond distribution, variation of reinforcing bar stress $\sigma_s(x)$ along the embedment length is defined as shown in Fig. 8b, where σ_y is the yield strength of steel and σ_h is the stress at the end of the straight part of the rebar anchorage. Then, by assigning an appropriate constitutive material law for steel [23], strain distribution $\varepsilon_s(x)$ is determined, as shown in Fig. 8c, where ε_y and ε_{sh} are the steel strains at the onset of yielding and strain hardening, respectively, and ε_h is the steel strain at the end of the straight part of the anchorage. It is important to note that post-yield nonlinearity of the material constitutive law, i.e. strain hardening, should be taken into account because it affects significantly the final results [11].

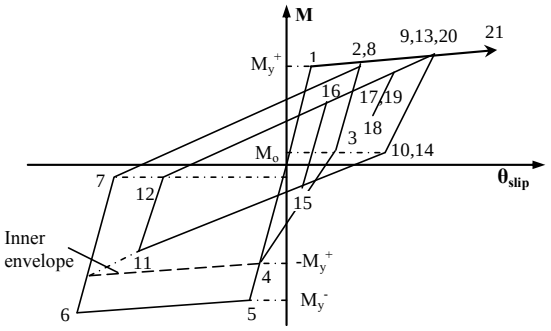

Fig. 9 M-θ_{slip} hysteretic model

Once $\varepsilon_s(x)$ is determined, slip of the reinforcement δ_{slip} can be calculated by integration along the anchorage length of the bar. In the case of hooked bars, local slip of the hook should be added. This can be evaluated by the force acting on the hook $P_h=A_b\cdot\sigma_h$, where A_b is the area of the anchored bar, and an appropriate hook force vs. hook slip constitutive relationship [24].

Upon determination of δ_{slip}, the respective fixed-end rotation can be calculated by Eq. 10, where $(d-x_c)$ is the distance between the bar and the neutral axis. The envelope M-θ_{slip} curve constructed by the various points of the afore-described methodology is then idealized by a bilinear relationship for analysis purposes.

$$\theta_{slip} = \frac{\delta_{slip}}{d - x_c} \tag{10}$$

After establishing the envelope curve, bond-slip hysteretic behaviour (Fig. 9) is determined by adopting the respective phenomenological model of Saatcioglu and Alsiwat [25]. Additional features have been introduced by the writers to prevent numerical instabilities resulting in the implementation of the specific model in the framework of nonlinear analysis.

In R/C structures with substandard detailing, anchorage-bond failures cannot be precluded. In case of straight anchorages, bond failure takes place when the anchorage length demand L_{dem} reaches the available straight embedment length $L_{straight}$. Hence, Eq. (11) holds, where σ_{sb} is the bar stress at anchorage failure and d_b represents bar diameter. If σ_{sb} exceeds steel stress corresponding to flexural failure, then bond is not the critical mode of failure for the examined anchorage.

$$\begin{aligned} &\sigma_{sb} \le \sigma_y \rightarrow \sigma_{sb} = \frac{4 \cdot \tau_{be'}}{d_b} \cdot L_{straight} \\ &\sigma_{sb} > \sigma_y \rightarrow \sigma_{sb} = \sigma_y + \frac{4 \cdot \tau_{bf}}{d_b} \cdot \left(L_{straight} - L_{pc} - \frac{\sigma_y \cdot d_b}{4 \cdot \tau_{be}} \right) \end{aligned} \tag{11}$$

In Eq. 11, $\tau_{be'}$ is a uniform bond strength higher than τ_{be} in order to consider the fact that for very short embedment lengths, where bond failure takes place for $\sigma_s<\sigma_y$, experimental evidence [21] shows that uniform bond strength τ_{be} underestimates significantly the available anchorage capacity. To avoid over-conservative solutions, it is proposed herein that $\tau_{be'}$ is taken by linear interpolation for $L_{straight}$ between τ_{be} corresponding to $L_y=\sigma_y \cdot d_b/(4 \cdot \tau_{be})$ and the ultimate local bond capacity τ_{bu} [22] corresponding typically to anchorage length equal to $5d_b$.

In the case of deficient end hooks, anchorage failure may be assumed to develop when the force acting on the hook reaches ultimate hook capacity P_{hu}. By equilibrium, Eq. 12 holds for determining σ_{sb}, where $L_{sh}=(\sigma_{sb}-\sigma_y) \cdot d_b/(4 \cdot \tau_{bf})$ and $L_d=(L_{straight}-L_{pc}-L_{sh})$.

$$\begin{aligned} &\sigma_{sb} \le \sigma_y \rightarrow \sigma_{sb} = \frac{P_{hu} + \pi \cdot d_b \cdot \tau_{be} \cdot L_{straight}}{A_{sb}} \\ &\sigma_{sb} > \sigma_y \;\&\; L_d \ge 0 \rightarrow \sigma_{sb} = \sigma_y + \frac{4 \cdot \tau_{bf}}{d_b} \cdot \left(L_{straight} - L_{pc} - \frac{\left(A_{sb} \cdot \sigma_y - P_{hu} \right)}{\pi \cdot d_b \cdot \tau_{be}} \right) \\ &\sigma_{sb} > \sigma_y \;\&\; L_d < 0 \rightarrow \sigma_{sb} = \frac{P_{hu} + \pi \cdot d_b \cdot \tau_{bf} \cdot \left(L_{straight} - L_{pc} \right)}{A_{sb}} \end{aligned} \tag{12}$$

3 Numerical implementation

The finite element model, described above, requires additional modifications to the nonlinear analysis solution algorithms in order to be implemented with consistency. It is known that during nonlinear analysis the following equation is solved in incremental form.

$$K \cdot \Delta U = \Delta F \tag{13}$$

Where K is the overall tangent stiffness matrix of the structure, ΔU is the vector of unknown nodal displacement increments and ΔF is the vector of the applied external load increments. The element stiffness matrices K_e are first calculated at the element level and later assembled into K.

In the case of dynamic analysis, the equivalent dynamic stiffness and external load matrices must be formed. Herein, the solution of the incremental system is carried out using the unconditionally stable constant-average acceleration Newmark-Beta algorithm [26]. Viscous damping matrix is calculated by assigning the Rayleigh damping model with circular frequencies corresponding to the first and second mode of vibration.

The solution is performed assuming that the properties of the structure do not change during the analysis step. Since the stiffness of some elements is likely to change during the step t, the new configuration at $t+\Delta t$ may not satisfy equilibrium. If ΔF_{ln} is the force increment vector arising from the assumption of constant stiffness during Δt and ΔF_{nl} is the force increment vector determined by the element nonlinear hysteretic laws, then an unbalanced force vector ΔF_{ub} arises, given by the following equation

$$\Delta F_{ub} = \Delta F_{ln} - \Delta F_{n1} \tag{14}$$

Typically, in the nonlinear analysis scheme, this issue is resolved by applying the one step unbalanced force correction method [27]. According to this technique, the unbalanced force vector is subtracted from the right part of Eq. (13) at the next time step of analysis. Despite the fact that this procedure minimizes computational effort in nonlinear analysis, it cannot be applied with consistency for finite elements composed by different sub-elements connected in series like the one presented in this study.

Figure 10 presents determination of unbalanced forces produced by two different hysteretic laws ($F\text{-}v_1$ and $F\text{-}v_2$), which are deemed coupled in series. The two hysteretic relationships have different elastic (k_{T1} and k_{T2}) and post-elastic stiffness ($r_1 \cdot k_{T1}$ and $r_2 \cdot k_{T2}$). It can be easily extracted that for the same force increment ΔF_{ln} the restoring force increments ΔF_{nl1} and ΔF_{nl2} and consequently unbalanced forces ΔF_{ub1} and ΔF_{ub2} become different, resulting in loss of member equilibrium.

To overcome this problem, the ‘event to event’ solution strategy [28] is adopted herein. This method is computationally effective when multilinear models are ap-

plied to capture hysteretic response. In accordance with this procedure, the nonlinear response of the structure is subdivided into subsequent events, which mark the change of stiffness of the entire structure. Between these events, linear behaviour is considered. Hence, each analysis step is divided (when required) into sufficient number of sub-steps, until no event takes place during the last sub-step. For the finite element developed herein, as an event is prescribed every change in stiffness of all hysteretic responses of all three sub-elements of each beam-column model.

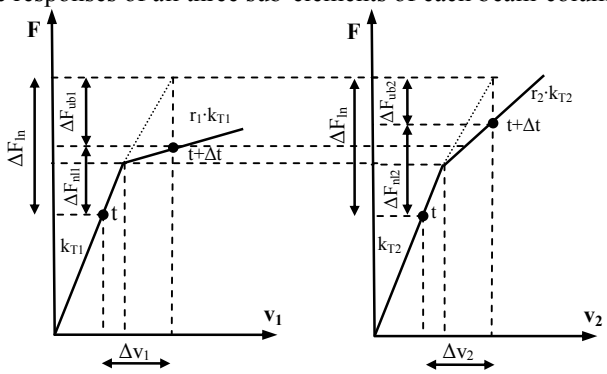

Fig. 10 Unbalanced forces for two hysteretic responses coupled in series

If the incremental load vector ΔF yields the deformation increment Δv_{mn} for the hysteretic response n of the element m, assuming constant stiffness, then the immediate next event force scale factor λ_{mn} corresponding to this hysteretic response is determined by

$$\lambda_{mn} = \min\left(1, \frac{v_{mne} - v_{mn}}{\Delta v_{mn}}\right) \tag{15}$$

In Eq. (15), v_{mne} is the deformation marking immediate next event and v_{mn} is the respective deformation at the beginning of the loading step. It is clear, that the immediate next event for the entire structure will correspond to the minimum value λ_{min} of all λ_{mn}. After calculating λ_{min}, the solution algorithm implemented to each nonlinear analysis step is presented in Fig. 11.

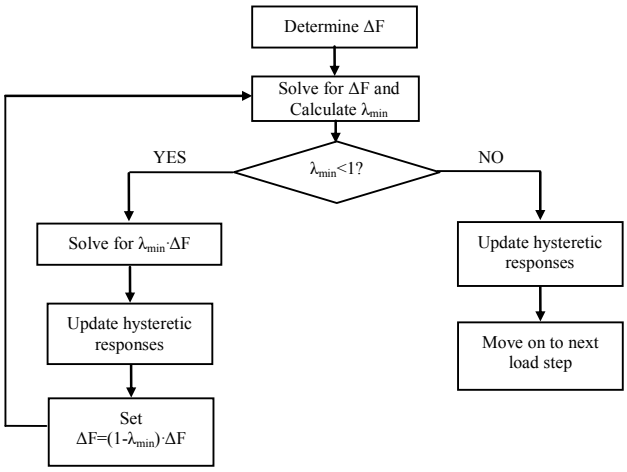

Fig. 11 Event to event solution algorithm

In addition to the above, following the procedure proposed in this study for determining tangent shear stiffness GA_{eff} after flexural yielding when accounting for shear-flexure interaction effect, it can be inferred by Eq. (7), that GA_{eff} becomes a function of the element shear force increment ΔV. But if it is to be applied in the analytical procedure, ΔV will be influenced by GA_{eff} as well, since the latter will affect the flexibility matrix of the element. To resolve this issue, an iterative analytical scheme, applied in the respective load step of the nonlinear analysis, is proposed herein, as detailed in the algorithm shown in Fig. 12.

Applying this procedure, it was found that numerical convergence is very fast. The number of iterations may increase as the influence of shear deformations on element flexibility enhances, but the additional computational cost required in this case is justified by the significance of calculating accurately shear response.

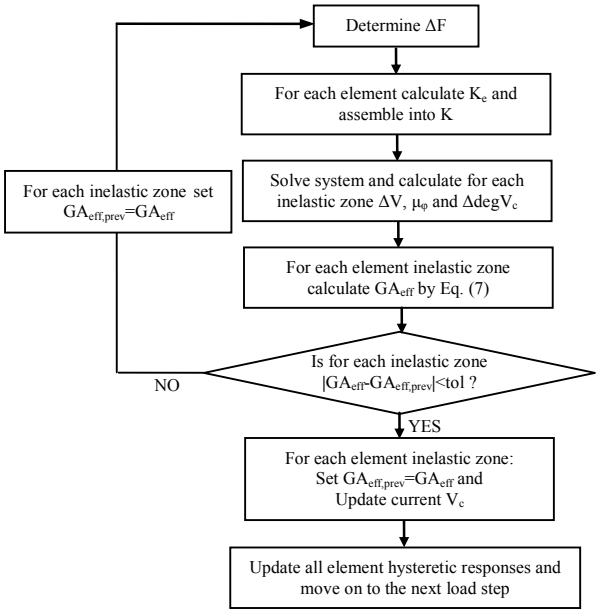

Fig. 12 Shear-flexure interaction implementation algorithm

4 Validation of the proposed model

The numerical model described above is implemented in the general finite element code IDARC2D developed at the State University of New York at Buffalo [29]. Then, it is validated against experimental results coming from well documented R/C column and frame specimens with substandard detailing.

In addition, parametric analyses reveal the necessity of incorporating each deformation mechanism in seismic assessment of 'old type' R/C structures in the linear and nonlinear range of response. To this purpose, each frame specimen is examined using four different beam-column models. The F model simulates only member flexural response. The FB model incorporates flexural and anchorage bond-slip response, while the FS one applies flexural and shear flexibility. Finally, the FSB model, which is the one proposed in this study, simulates all deformation mechanisms, as well as their interaction.

4.1 R/C beam specimen R5 by Ma et al. (1976)

Ma et al. [30] tested nine cantilever beams, representing half scale models of the lower story of a 20-storey ductile moment-resisting R/C office building. Herein, the specimen designated as R5 is examined. Shear span ratio was equal to 2.41. Longitudinal reinforcement consisted of 4 top and 4 bottom 19mm bars, while volumetric ratio of transverse reinforcement was set equal to 0.31%. Concrete strength was 31.5MPa and yield strengths of longitudinal and transverse rein-

forcement were 452MPa and 413MPa, respectively. The specimen was subjected to a cyclic concentrated load at the free end.

Figure 13 presents lateral load vs. lateral displacement response as derived by the proposed model and as recorded experimentally. It can be seen that the analytical model reproduces sufficiently the experimental initial stiffness, lateral load capacity, and unloading stiffness. Reloading stiffness is predicted well during the early phases of inelastic response. However, as displacement demand increases, the pinching effect is underestimated leading to a small overestimation of the energy dissipation capacity of the member. It is pointed out that the displacement level at which shear failure is predicted by the analytical model correlates sufficiently well with the onset of serious shear strength degradation in the experimental response ($\mu_{\Delta}\approx4$).

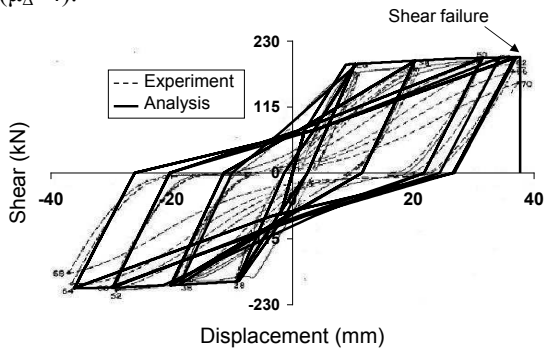

Fig. 13 Lateral load vs. total displacement response for specimen R5 (Ma et al. 1976)

Figure 14a compares shear strength predicted by Priestley's model [15] and acting shear force as a function of the end section curvature demand. Initially, shear capacity exceeds significantly shear demand. However, due to inelastic curvature development, at the end of the analysis shear demand reaches shear capacity marking the onset of stirrup yielding. Maximum curvature demand is well predicted (experiment 0.11rad/m and prediction 0.12rad/m).

Figure 14b shows moment vs. fixed-end rotation hysteretic response caused by anchorage slippage as derived by the analytical model described in this study. Maximum rotation is predicted equal to 0.007rad in both directions.

Figure 14c illustrates shear hysteretic response inside the plastic hinge region as predicted by the analytical model. It is obvious that this relationship is characterised by intense pinching effect following the hysteretic model proposed in [18]. The predicted behaviour matches adequately the experimental response with slight underestimation of the observed pinching effect [30]. Shear deformation at onset of shear failure is calculated equal to 0.043 and is in close agreement with the experimental evidence [30].

In Fig. 14c, V-γ envelope without shear-flexure interaction is also included. At the beginning, the initial envelope determines shear hysteretic response. Nevertheless, as soon as $\mu_{\varphi}>3$, shear deformations increase more rapidly, due to interaction with flexure, and shear hysteresis separates from the initial skeleton curve. After

stirrup yielding, occurring for $\gamma \approx 4‰$, shear rigidity becomes close to zero and V-γ skeleton curve including shear-flexure interaction continues in parallel with the initial envelope.

In Fig. 14d, variation of displacement components with μ_Δ is presented as derived by the proposed model and experimental recordings. It can be seen that the analytical and experimental displacement patterns are in close agreement. Although shear demand after flexural yielding remains almost constant, analytically derived shear displacement increases significantly due to modelling interaction with flexure and subsequent stirrup yielding.

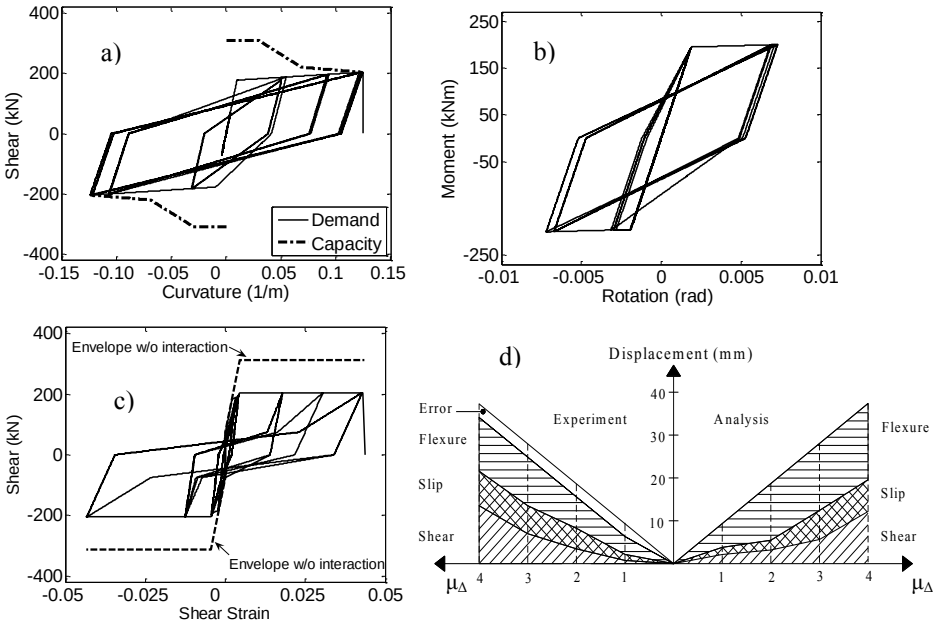

Fig. 14 (a) Shear demand and capacity as a function of the end section curvature demand. (b) Analytical M-θ_{slip} hysteresis. (c) Analytical V-γ relationship inside the plastic hinge region. (d) Variation of member displacement components with μ_Δ demand as predicted by the analytical model and measured experimentally

4.2 R/C bridge pier specimen HS2 by Ranzo and Priestley (2001)

Ranzo and Priestley [31] tested three thin-walled circular hollow columns. Herein, the specimen designated as HS2 is examined, which was designed to fail in shear after yielding in flexure. Its outer diameter was 1524mm and wall thickness 139mm. The ratio of the column shear span to the section outer diameter was equal to 2.5. The normalised applied compressive axial load was 0.05. Longitudinal reinforcement ratio was 2.3% and the volumetric ratio of transverse reinforcement 0.35%. Concrete strength was 40MPa and yield strengths of longitudinal and transverse reinforcement were 450MPa and 635MPa, respectively. Lateral actions

were applied in the push and pull direction of the column for increasing levels of displacement ductility μ_Δ with three repeated cycles at each μ_Δ.

Figure 15a shows the experimental and analytical lateral load vs. total displacement response of the specimen. The analytical model captures accurately the initial stiffness, lateral strength and hysteretic response of the R/C member. More importantly, the proposed model is able to predict reasonably well the tip displacement at which onset of shear failure is developed.

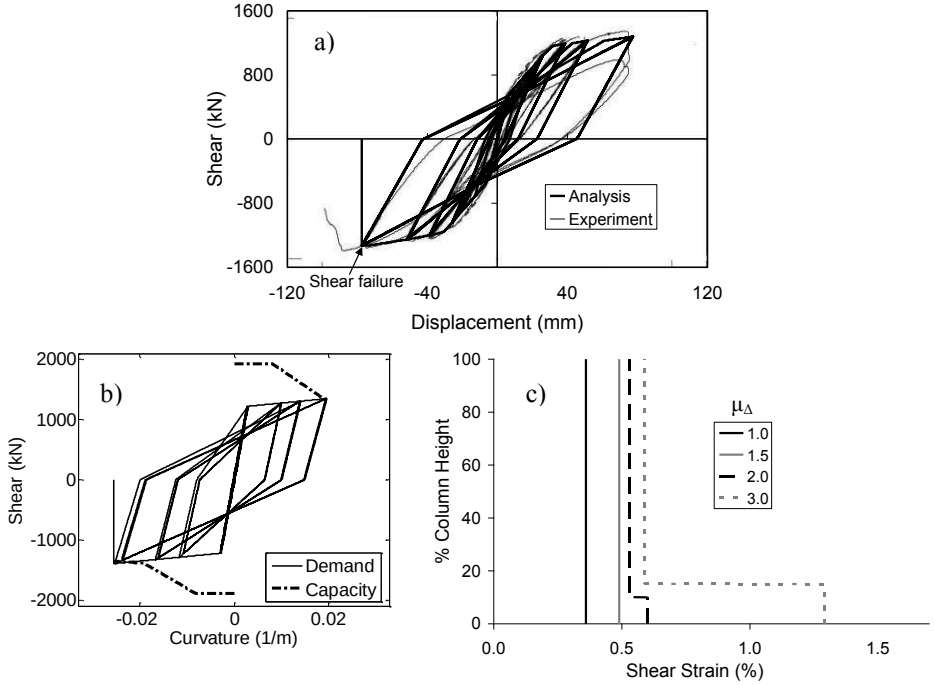

Fig. 15 (a) Specimen HS2 (Ranzo & Priestley 2001). (a) Lateral load vs. total displacement response. (b) Shear demand and capacity as a function of the end section curvature demand. (c) Shear strain distribution for increasing displacement ductility demands

This can be seen also in Fig. 15b, which compares shear strength given by Priestley's model and acting shear force as a function of the end section curvature demand. Initially, shear capacity exceeds significantly shear demand. However, due to inelastic curvature development, at the end of the analysis shear demand reaches shear capacity marking the onset of stirrup yielding. It is worth reporting that maximum curvatures predicted by the analytical model (0.019rad/m and 0.025rad/m in positive and negative bending respectively) correlate sufficiently with the measured ones inside the plastic hinge region (approx. 0.02rad/m) [31].

Fig. 15c illustrates shear strain distribution of the R/C column as predicted by the proposed shear sub-element for various levels of increasing μ_Δ. For μ_Δ=1.0, shear strains remain constant along the height of the member. After $\mu_\Delta \geq 1.5$, a double effect is noted: First, shear strains in the inelastic zone increase more rapidly

and tend to differ substantially from the ones in the intermediate part of the element due to shear-flexure interaction effect and consequent yielding of transverse reinforcement. Second, the length of the inelastic zone increases following expansion of flexural yielding towards the mid-span. By this combined effect, gradual spread of inelastic shear deformations is appropriately captured by the proposed model. At the onset of shear failure, occurring inside the plastic hinge, shear deformations are predicted equal to 0.3% and 1.3% outside and inside the inelastic zone, respectively. Both of these values are in good agreement with the experimental results (approx. 0.3% and 1.2% respectively) [31].

4.3 R/C frame specimen by Duong et al. (2007)

This one bay, two storeys frame (Fig. 16a) was tested by Duong et al. [32] at University of Toronto. The frame was subjected to a single cycle loading. During the experiment, a lateral load was applied to the second storey beam in a displacement controlled mode, while two constant axial loads were applied to simulate the axial load effects of higher stories (Fig. 16a). During loading sequence, the two beams of the frame experienced significant shear damage (close to shear failure) following flexural yielding at their ends [32].

The finite element model applied herein for the inelastic cyclic static analysis of the frame is also shown in Fig. 16a. It consists of 4 column elements and 2 beam elements (one for each column and beam). Hence, the number of finite elements applied is minimum assuring high computational efficiency to the numerical model. The columns are supposed to be fixed at the foundation. Rigid arms are employed to model the joints of the frame.

Figures 16b, 16c compare the experimental and analytical top displacement and base shear responses obtained by the F (flexure), FB (flexure-bond) and FSB (flexure-shear-bond) finite element models. As shown in Fig. 16b, the FSB model follows closely the experimental behaviour in the whole range of response. Slight underestimation of the frame lateral stiffness takes place at the early stages of loading. This is due to the fact that pre-cracking flexural response is not modelled in this study. However, the following gradual decrease of frame stiffness is sufficiently captured by the analytical model.

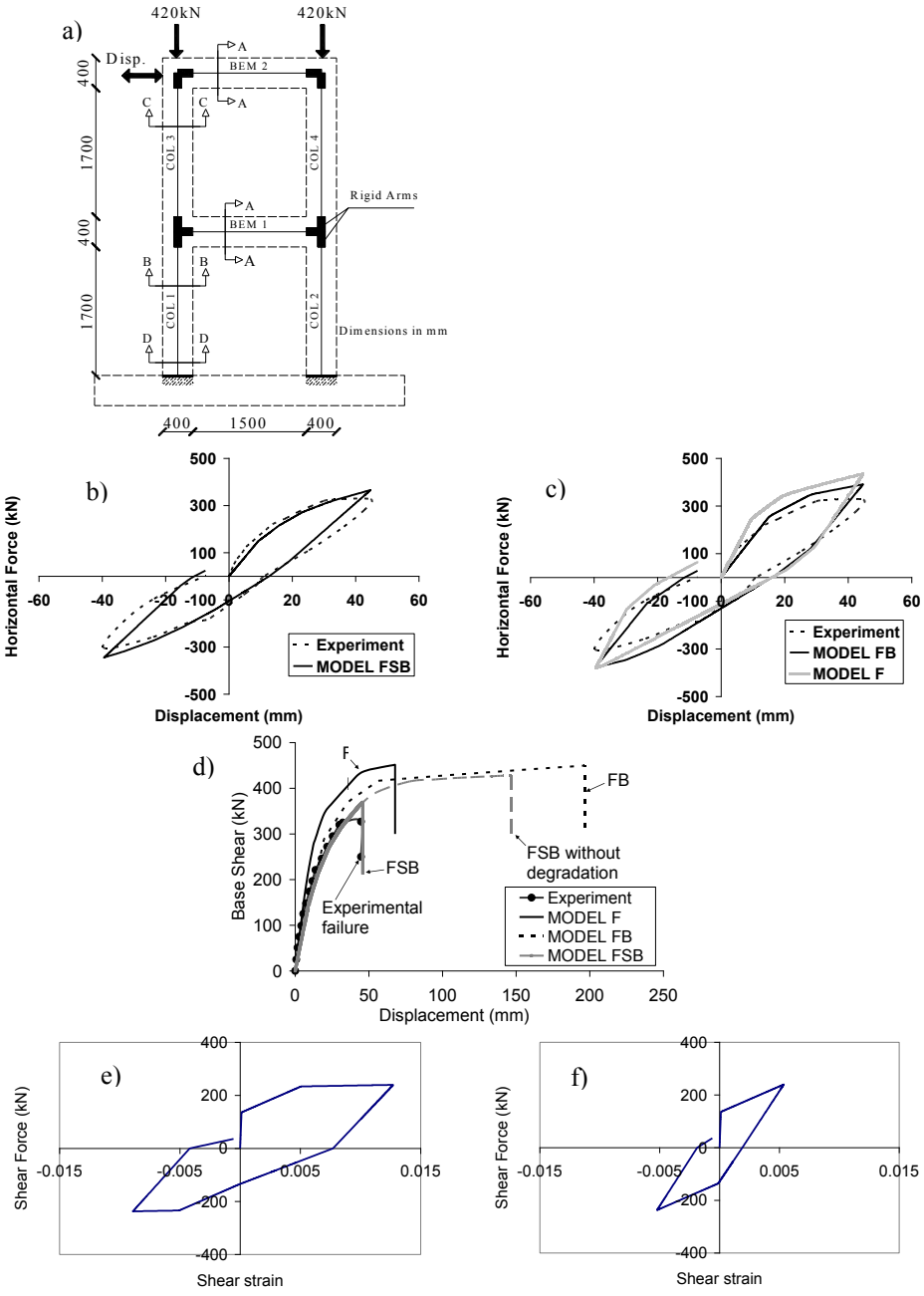

Fig. 16 (a) Duong et al. frame specimen layout and applied finite element model. (b) Base shear vs. top displacement prediction by FSB model. (c) Base shear vs. top displacement predictions by F and FB models. (d) Pushover curves from different finite element models. (e) First storey beam V-γ response inside plastic hinges. (f) First storey beam V-γ response outside plastic hinges

At maximum displacement, the analytical model slightly overestimates load capacity (having a calculated-to-observed ratio of 1.10 in both directions). Furthermore, the analytical model predicts correctly that both beams develop shear failures after yielding in flexure.

On the other hand, the F and FB models considerably overestimate the stiffness and load carrying capacity and consequently the ability of the examined frame to dissipate hysteretic energy. For the F model, the load carrying capacity calculated-to-observed ratio is 1.30 and 1.23 in the positive and negative direction respectively. The prediction is improved with inclusion of anchorage slip effect in the FB model and the aforementioned ratio becomes 1.19 and 1.22 in the positive and negative direction.

Figure 16d presents the pushover curves obtained by the different finite element models. It can be seen that the F and FB models overestimate stiffness, load and displacement capacity. At the end of the analysis, the F and FB models overestimate load carrying capacity by 38% and 37% respectively. The same models overestimate displacement capacity by 52% and 358% accordingly. Both models erroneously predict flexural failure at the base of the frame.

The FSB model predicts correctly that shear failure is developed after yielding in flexure. However, inclusion of shear-flexure interaction effect and degradation of shear strength with curvature ductility demand affects grossly the displacement capacity predicted by this analytical model. When shear-flexure interaction is considered, ultimate displacement capacity is found 46mm which is very close to the 44.7mm recorded experimentally. On the other hand, if shear-flexure interaction is ignored, displacement capacity is overestimated by 228%.

Finally, Figs 16e and 16f present shear force – shear strain hysteresis predicted by the FSB analytical model inside and outside the plastic hinge regions for the 1st storey beam of the frame under cyclic loading. It can be seen that, due to shear-flexure interaction effect and consequent stirrup yielding, shear strains are predicted significantly higher inside than outside plastic hinges (1.26% instead of 0.53%), while shear force remains uniform along this RC member.

4.4 R/C frame specimen by Elwoood and Moehle (2008)

This half-scale frame specimen was constructed and tested on the shaking table at the University of California, Berkeley [6]. It comprised three columns interconnected at the top by a 1.5m wide beam and supported at the bottom on footings (Fig. 17a). The columns supported a total mass of 31t.

The central column was constructed with light transverse reinforcement having 90^o hooks. The outside columns were detailed with closely spaced spiral reinforcement to ensure ductile response and to provide support for gravity loads after shear failure of the central column.

The specimen was subjected to one horizontal component of the ground motion recorded at Viña del Mar during the 1985 Chile earthquake (SE32 component). The normalized central column axial load was 0.10. During testing, the central

column experienced a loss of lateral load capacity, due to apparent shear failure at its top, during a negative displacement cycle at approximately 17.6sec [6].

The finite element model applied herein for the inelastic time history analysis of the frame is shown in Fig. 17a. It consists of 3 column elements and 2 beam elements (one for each member). Hence, the number of finite elements required is minimum assuring minimum computational cost.

The columns are supposed to be fixed at the foundation. Rigid arms are employed to model the joints of the frame. Rayleigh model is used for viscous damping. The equivalent viscous damping is set equal to 2% of the critical damping for the fundamental vibration mode. The mass is assumed lumped at the top of the frame. In the following, for the calculation of the central column shear strength, the contribution of the stirrups is reduced by half to take into account their inadequate anchorage (90^o hooks).

Figures 17b, 17c compare the experimental and the analytical top displacement time histories between t=10sec and onset of shear failure as predicted by the FSB and F analytical models respectively. The first 10 seconds are omitted so that the critical duration of response can be more clearly observed [6]. It is evident that the FSB analytical model predicts closely the experimental response up to onset of shear failure of the central column. On the other hand, when only flexural deformations are considered (which is the typical case for conventional inelastic analyses of R/C structures) the analysis is driven to severely erroneous results.

In addition, Fig. 17d presents the comparison between the experimental and analytical frame hysteresis up to onset of shear failure as predicted by the FSB model. It is apparent that the model captures satisfactorily initial frame stiffness, maximum shear capacity and displacement corresponding to onset of shear failure.

Finally, Fig. 17e compares the pushover curves obtained by the four different versions of the beam-column model and the experimental response. The comparison is shown in the negative displacement direction because in this direction shear failure was detected.

The F model significantly overestimates initial frame stiffness and underestimates displacement at failure. In particular, this model predicts erroneously flexural failure at the base of the central column at a 20mm lateral displacement.

The FS model predicts correctly the development of shear failure at the top of central column. However, it overestimates initial lateral stiffness and underestimates displacement capacity at onset of shear failure (27mm instead of 51mm).

The FB model provides better estimations than the two previous models. However, it overestimates frame stiffness after base shear exceeds 150kN (onset of shear cracking) and underestimates considerably displacement at onset of lateral failure (37mm instead of 51mm). Moreover, a flexural failure at the base of the central column is falsely predicted.

The best estimations are provided by the FSB model which incorporates all types of deformations and represents the proposal of this study. Envelope stiffness is closely captured until maximum response. Additionally, this model predicts correctly a shear failure at the top of the central column at a 47mm displacement, which is quite close to the experimental value.

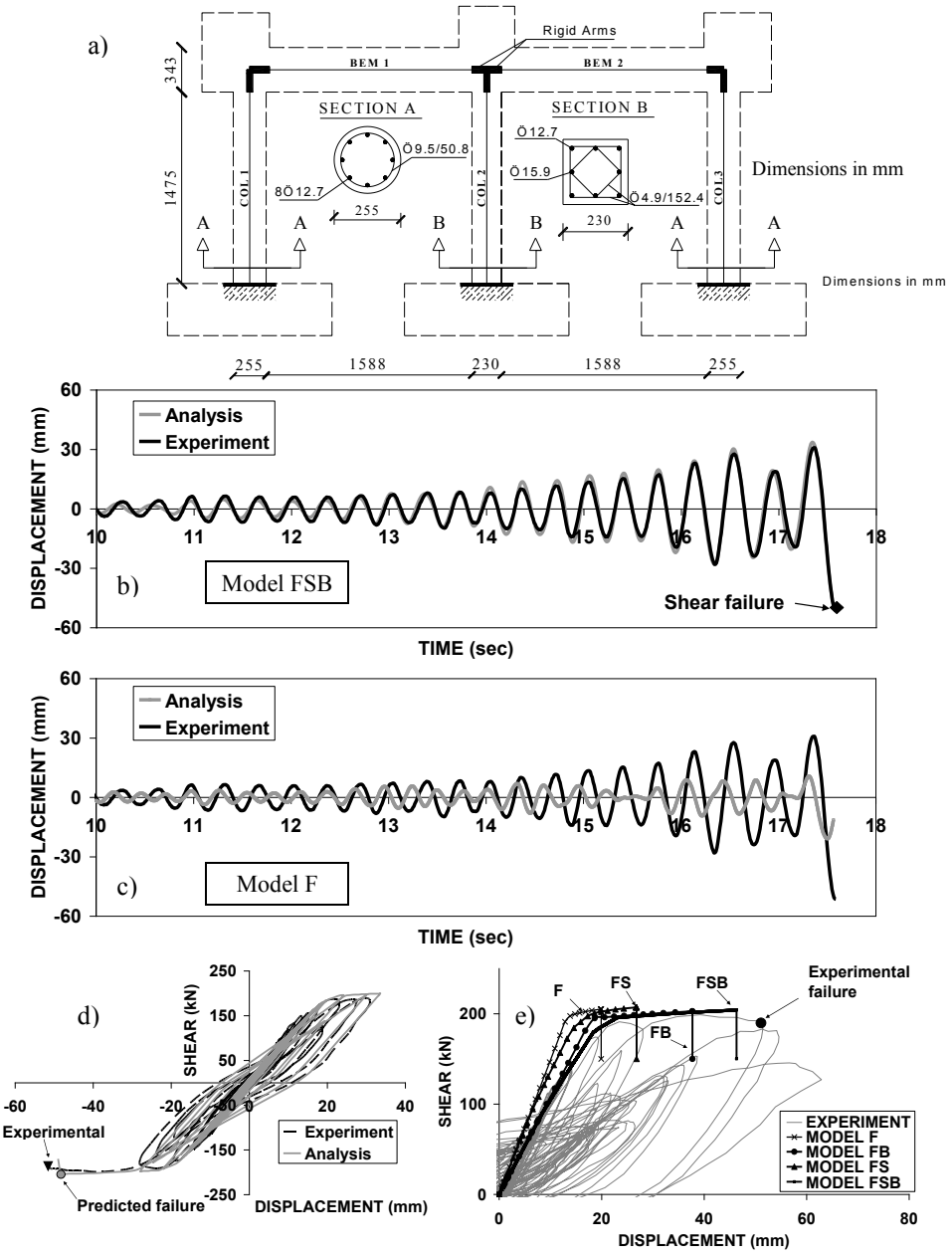

Fig. 17 (a) Elwood & Moehle frame specimen layout and applied finite element model. (b) Displacement time history predicted by FSB model. (c) Displacement time history predicted by F model. (d) Frame hysteresis predicted by FSB model. (e) Pushover curves from F, FB, FS and FSB finite element models and comparison with the experimental response

4.5 R/C frame specimen by El-Attar et al. (1997)

A 1/6 scale 2-storey one-bay by one-bay reinforced concrete building (Fig. 18) was tested at the Cornell University [33]. The structure was designed solely for gravity loads, without regard to any kind of lateral loads. Model structure concrete strength was 32.3MPa and steel reinforcement yield capacity 414MPa.

The model structure was tested using the time-scaled Taft 1952 S69E earthquake with peak ground acceleration set in increasingly higher values. After running Taft 0.45g, wide, deep cracks were observed in the beams around the locations of discontinuous positive beam reinforcement (at the joint panels), indicating bond failure and pending pullout of these bars [33].

Figure 19 compares frame response histories derived by the FSB analytical model and experimental recordings for the 0.36g peak ground acceleration. It is evident that the proposed model follows closely the experimental response after the first 1.5sec. Small differentiations are justifiable considering the large scale (1/6) of the examined specimen.

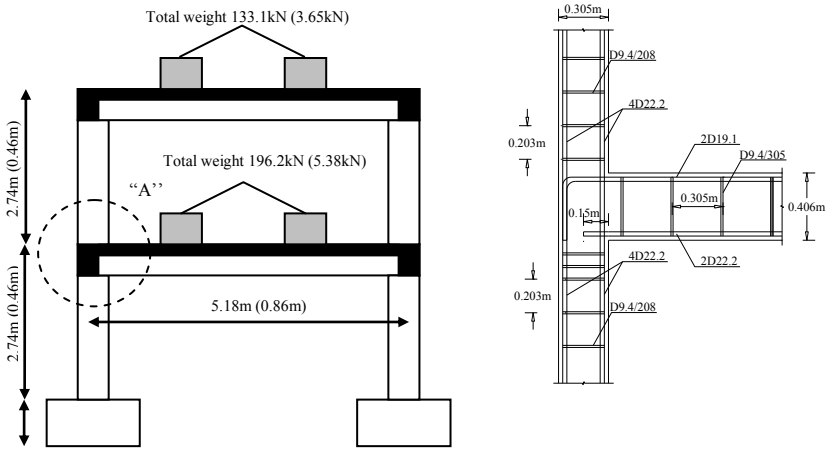

Fig. 18 (a) El-Attar et al. (1997) frame specimen configuration (values outside and inside parentheses correspon

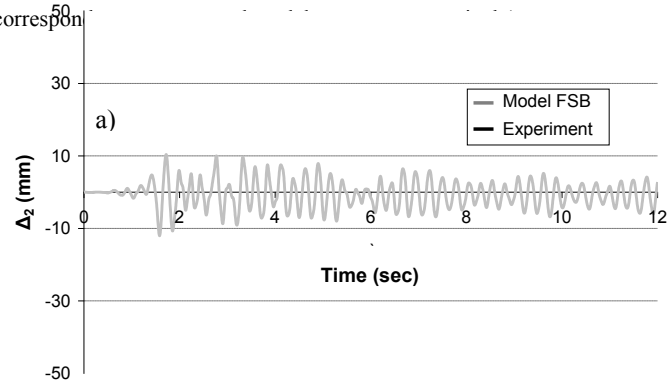

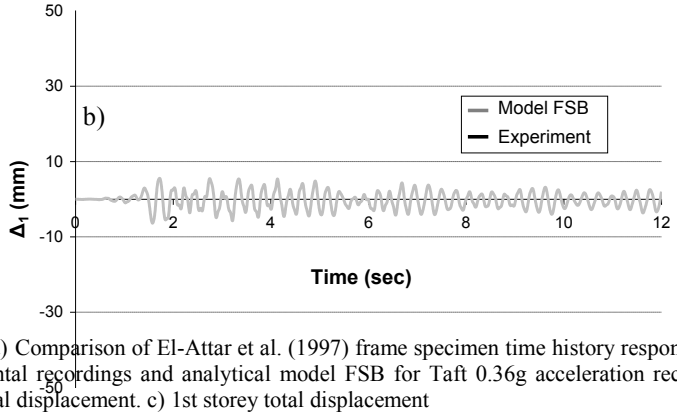

Fig. 19 (a) Comparison of El-Attar et al. (1997) frame specimen time history responses from the experimental recordings and analytical model FSB for Taft 0.36g acceleration record. (a) 2nd storey total displacement. c) 1st storey total displacement

The FSB analytical model predicts the anchorage failure of the positive reinforcement at the left end of the first storey beam for the 0.45g Taft earthquake motion. This is clear by Fig. 20 presenting hysteretic M-φ and M-θ_{slip} responses of this end. It can be seen that while flexural response remains at the reloading stage, M-θ_{slip} concludes the reloading branch, moves on to the positive envelope curve and finally drives to failure, exceeding bottom anchorage moment capacity.

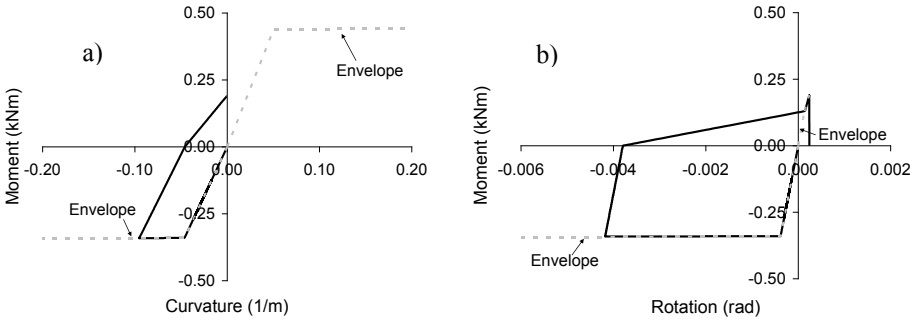

Fig. 20 Hysteretic responses of left end of the 1st storey beam of the El-Attar et al. (1997) frame specimen predicted by the FSB analytical model for the 0.45g Taft acceleration record. (a) M-φ. (b) M-θ_{slip}

5 Conclusions

A new beam-column model is introduced for seismic damage analysis of R/C frame structures with substandard detailing. This finite element models inelastic flexural, shear, and anchorage slip deformations, as well as their interaction, in an explicit manner. Hence, it is capable of simulating with accuracy the seismic response of R/C frames with inadequate detailing, where shear flexibility and fixed end rotations caused by anchorage slip usually play a vital role in their response. Additionally, it is able to predict, in the general case, brittle types of failure that cannot be precluded in structures, which do not conform to modern seismic guidelines. The numerical model is implemented in a general finite element code and it

is validated against experimental results from well-documented column and frame specimens with brittle detailing. It is concluded that the proposed model provides accurate and reliable predictions of the frame specimen responses.

References

[1] Mergos PE, Kappos AJ (2010) Seismic damage analysis including inelastic shear-flexure interaction. Bull Earthquake Eng 8:27-46

[2] CEN (Comité Européen de Normalisation) Eurocode 8 (2005) Design provisions of structures for earthquake resistance - Part 3: Assessment and retrofitting of buildings (EN1998-3), Brussels

[3] Pincheira J, Dotiwala F, Souza J (1999) Seismic analysis of older reinforced concrete columns. Earthquake Spectra 15:245-272

[4] Consenza E, Manfredi G, Verderame GM (2002) Seismic assessment of gravity load designed R/C frames: Critical issues in structural modelling. J Earthquake Eng 6:101-122

[5] Yalcin C, Saatcioglu M (2000) Inelastic analysis of reinforced concrete columns. Computers and Structures 77: 539-555

[6] Elwood K, Moehle J (2008) Dynamic collapse analysis for a reinforced concrete frame sustaining shear and axial failures. Earthquake Eng Struct Dyn 37:991-1012

[7] Sezen H, Chowdhury T (2009) Hysteretic model for reinforced concrete columns including the effect of shear and axial load failure. J Struct Eng 135:139-146

[8] Mergos PE, Kappos AJ (2008) A distributed shear and flexural flexibility model with shear-flexure interaction for R/C members subjected to seismic loading. Earthquake Eng Struct Dyn 37:1349-1370

[9] Mergos PE, Kappos AJ (2009) Modelling gradual spread of inelastic flexural, shear and bond-slip deformations and their interaction in plastic hinge regions of R/C members. In: Proc. of the 2nd COMPDYN Conference, Rhodes, Greece

[10] Mergos PE, Kappos AJ (2011) Seismic damage analysis of RC structures with sub-standard detailing. Proc. of the 3rd COMPDYN Conference, Corfu, Greece

[11] Mergos PE, Kappos AJ (2012) A gradual spread inelasticity model for R/C beam-columns accounting for flexure, shear and anchorage slip. Eng Struct 44:94-106

[12] Sivaselvan MV, Reinhorn AM (1999) Hysteretic model for cyclic behaviour of deteriorating inelastic structures. Report MCEER-99-0018, University at Buffalo, State Univ. of New York

[13] Soleimani D, Popov EP, Bertero VV (1979) Nonlinear beam model for R/C frame analysis. In: Proc. of 7th Conference on Electronic Computation, St. Louis, Missouri

[14] Sezen H, Moehle JP (2004) Shear strength model for lightly reinforced concrete columns. J Struct Eng 130:1692-1703

[15] Priestley MJN, Seible F, Verma R, Xiao Y (1993) Seismic shear strength of reinforced concrete columns. Report No. SSRP-93/06, University of San Diego, California

[16] Biskinis D, Roupakias G, Fardis MN (2004) Degradation of shear strength of R/C members with inelastic cyclic displacements. ACI Struct J 101:773-783

[17] Oesterle RG, Fiorato AE, Aristizabal-Ochoa JD (1980) Hysteretic response of reinforced concrete structural walls. In: Proc. ACISP-63: Reinforced Concrete Structures subjected to Wind and Earthquake Forces, Detroit

[18] Ozcebe G, Saatcioglu M (1989) Hysteretic shear model for reinforced concrete members. J Struct Eng 115:132-148

[19] Park R, Paulay T (1975) Reinforced concrete structures. Wiley and Sons, New York

[20] Alsiwat JM, Saatcioglu M (1992) Reinforcement anchorage slip under monotonic loading. J Struct Eng 118:2421-2438

[21] ACI Committee 408 (2003) Bond and development of straight reinforcement in tension. American Concrete Institute, Farmington Hills

[22] CEB-FIP Model Code (1990) Model code for seismic design of concrete structures. Lausanne

[23] Park R, Sampson RA (1972) Ductility of reinforced concrete column sections in seismic design. ACI Struct J 69:543-551

[24] Soroushian P, Kienuwa O, Nagi M, Rojas M (1988) Pullout behaviour of hooked bars in exterior beam-column connections. ACI Struct J 85:269-276

[25] Saatcioglu M, Alsiwat JM, Ozcebe G (1992) Hysteretic behaviour of anchorage slip in R/C members. J Struct Eng, 118:2439-2458

[26] Newmark NM (1959) A method of computation for structural dynamics. J Eng Mechanics Division 89:67-94

[27] Kanaan AE, Powel GH (1973) DRAIN-2D: A general purpose computer program for dynamic analysis of inelastic plane structures. Report EERC-73/06 and 73/22, Univ. of California Berkeley

[28] Golafshani AA (1982) DRAIN-2D2: A program for inelastic seismic response of structures. PhD Dissertation, Dept. of Civil Engineering, Univ. of California Berkeley

[29] Reinhorn AM, Roh H, Sivaselvan M et al. (2009) IDARC2D Version 7.0: A program for the inelastic damage analysis of buildings. Report MCEER-09-0006, University at Buffalo, State Univ. of New York

[30] Ma SM, Bertero VV, Popov EP (1976) Experimental and analytical studies on hysteretic behaviour of R/C rectangular and T-beams. Report EERC 76-2. Univ of California Berkeley

[31] Ranzo G, Priestley MJN (2001) Seismic performance of circular hollow columns subjected to high shear. Report No. SSRP-2001/01, Univ. of California San Diego

[32] Duong KV, Sheikh SA, Vecchio FJ (2007) Seismic behaviour of shear critical reinforced concrete frame: Experimental Investigation. ACI Struct J, 104:304-313

[33] El-Attar AG, White RN, Gergely P (1997) Behaviour of gravity load designed R/C buildings subjected to earthquakes. ACI Struct J 94:1-13